Supporting Information for

A redox active rod coordination polymer from tetrakis(4-carboxylic acid biphenyl)tetrathiafulvalene

Nicolas Zigon,*[,a] Federica Solano,[a] Pascale Auban-Senzier,[b] Stéphane Grolleau,[c] Thomas Devic,[c] Pavel N. Zolotarev,[d] Davide M. Proserpio,[d] Bolesław Barszcz,[e] Iwona Olejniczak,[e] Narcis Avarvari*[,a]

[a] Univ Angers, CNRS, MOLTECH-ANJOU, SFR MATRIX, F-49000 Angers, France. E-mail: narcis.avarvari@univ-angers.fr; nicolas.zigon@univ-angers.fr

[b] Université Paris-Saclay, CNRS, UMR 8502, Laboratoire de Physique des Solides, 91405 Orsay, France

[c] Université de Nantes, CNRS, Institut des Matériaux Jean Rouxel, IMN, F-44000 Nantes, France

[d] Università degli studi di Milano, Dipartimento di Chimica, Via Golgi 19, 20133 Milano, Italy

[e] Institute of Molecular Physics, Polish Academy of Sciences, Smoluchowskiego 17, 60-179 Poznań, Poland

SUMMARY

X-Ray structure determinations

Details about data collection and solution refinement are given in Table S1. Data collections were performed on a Rigaku Oxford Diffraction SuperNova diffractometer equipped with an Atlas CCD detector and micro-focus Cu-K_α radiation (λ = 1.54184 Å). The structures were solved by intrinsic phasing and refined on F^2 by full matrix least-squares techniques with SHELX programs (SHELXT 2018/2 and SHELXL 2018/3)[1,2] using the ShelXle and the Olex2 graphical user interfaces.[3,4] All non-H atoms were refined anisotropically and absorption was corrected by multiscan empirical absorption using spherical harmonics with CrysAlisPro program. The H atoms were placed at calculated positions and refined using a riding model. Crystallographic data for the two structures have been deposited with the Cambridge Crystallographic Data Centre, deposition numbers CCDC 2300287 for **1-Me$_4$**, 2300286 for **1-Zn$_2$**. These data can be obtained free of charge from CCDC, 12 Union road, Cambridge CB2 1EZ, UK (e-mail: deposit@ccdc.cam.ac.uk or http://www.ccdc.cam.ac.uk).

Powder X-Ray diffraction (PXRD)

Measurements were done on a D8 Bruker diffractometer (CuKα, λ = 1.5418 Å) equipped with a linear Vantec super speed detector. The data were processed with the EVA software, the Cu$K\alpha_2$ radiation and the background were removed.

Solid state cyclic voltammetry

To measure solid state electrochemical behaviour of PCPs, a cylindrical Teflon cell featuring a hole (0.4 cm diameter) in the bottom was used in a vertical configuration, where a glassy carbon plate as working electrode, WE, was tightened from below. The cell was tightened on a copper plate as the electrical contact. A Pt wire and Ag wire were used as counter electrode (CE) and reference electrode (RE) respectively and placed at the top of the cylinder in contact with the electrolytic solution (0.1M $TBAPF_6$in AN) vs *Fc+/Fc*. The PCPs were placed over the WE and covered with a Nafion membrane, to prevent direct contact between the solid MOFs and the electrolytic solution.

Thermo-gravimetric analysis

TGA was performed on a NETZCH TG209 F3-Tarsus apparatus, under a N_2 flow in a Platinum crucible, with a 10 K/min scan rate.

Infrared measurements

IR measurements were done on a BRUKER Vertex70 FTIR equipped with a diamond ATR. Spectra were corrected for H_2O and CO_2.

Raman measurements

Raman spectra were measured in a backward scattering geometry using a Raman LABRAM HR800 spectrometer equipped with a microscope and He-Ne laser excitation $\lambda = 632.8$ nm. The spectra were recorded at room temperature with a spectral resolution of 2 cm^{-1} and power reduced to approximately 0.3 mW to avoid sample overheating.

Table S1. Crystallographic data, details of data collection and structure refinement parameters.

	1-Me$_4$	**1-Zn$_2$**
Formula sum	$C_{62}H_{44}O_8S_4$	$C_{58}H_{32}O_8S_4Zn_2$, 2(C_4H_9NO)
Formula weight	1045.21	1290.06
Crystal system	Triclinic	Monoclinic
Space group	*P*-1	*C*2/m
a/Å	9.0464(6)	5.8818(3)
b/Å	16.8087(8)	34.912(2)
c/Å	21.6001(11)	18.5705(12)
α/°	69.636(5)	90
β/°	85.008(5)	97.076(6)
γ/°	75.340(5)	90
V/Å^3	2978.9(3)	3784.3(4)
Z	2	2
D_c/g cm^{-3}	1.165	1.132
T/K	295	150
μ/mm^{-1}	1.870	2.210
Reflections collected	11155	3615
Independent reflection	7106	2574
final $R_1{}^a$, $wR_2{}^b$ [$I > 2\sigma(I)$]	0.0565/0.1493	0.0548/0.1455
$R_1{}^a$,$wR_2{}^b$ (all data)	0.0849/0.1733	0.0748/0.1595
goodness-of-fit on F^2	0.975	1.049
$\Delta\rho_{min}/\Delta\rho_{max}$ (e Å^{-3})	-0.274/0.238	-0.552/0.406
Completeness (%)	97.9	98.4
CCDC number	2300287	2300286

[a] $R_1 = \sum||F_o|-|F_c||/\sum|F_o|$. [b] $wR_2 = [\sum w(F_o^2 - F_c^2)^2/\sum w(F_o^2)^2]^{1/2}$; $w = 1/[\sigma^2(F_0^2)+(aP)^2+bP]$ where $P= [max(F_0^2, 0) + 2F_c^2]/3$.

Table S2. List of the six networks with the **sqc1121** net topology in the PE&M representation analogous to **1-Zn_2**. Void space was computed with PLATON after the removal of the solvent molecules.

CSD Identifier	Formula	Solvent accessible voids	Complete name	Reference
AVIMIC	$C_{32}H_{21}N_1O_{10}Zn_2$	18% voids	5,5'-[biphenyl-4,4'-diylbismethanediyloxy]dibenzene-1,3-dicarboxylato-di-zinc acetonitrile solvate	[5]
AJIFIJ	$C_{16}H_{24}Cd_4O_{22}$	*Non porous*	Butane-1,2,3,4-tetracarboxylato-hexa-aqua-di-cadmium	[6]
RUNXUV	$C_{40}H_{48}N_4O_{13}Zn_2$	38% voids	4,4',4'',4'''-Ethane-1,2-diylbisnitrilobismethylenetetrabenzoato-di-zinc N,N-dimethylformamide solvate trihydrate	[7]
CAZLEV	$C_4H_{10}Ag_2O_6P_2$	*Non porous*	Butane-1,4-diphosphonato-di-silver	[8]
DEXKEZ	$C_{23}H_{17}Mn_2N_3O_{13}$	*Non porous*	5,5'-[pyridine-3,5-diylbiscarbonylazanediyl]dibenzene-1,3-dicarboxylato-diaqua-di-manganese monohydrate	[9]
QOKCID	$C_{24}H_{16}O_{11}Zn_2$	13% voids	5,5'-1,3-Phenylenebismethylenebisoxydi-isophthalato-di-zinc monohydrate	[10]

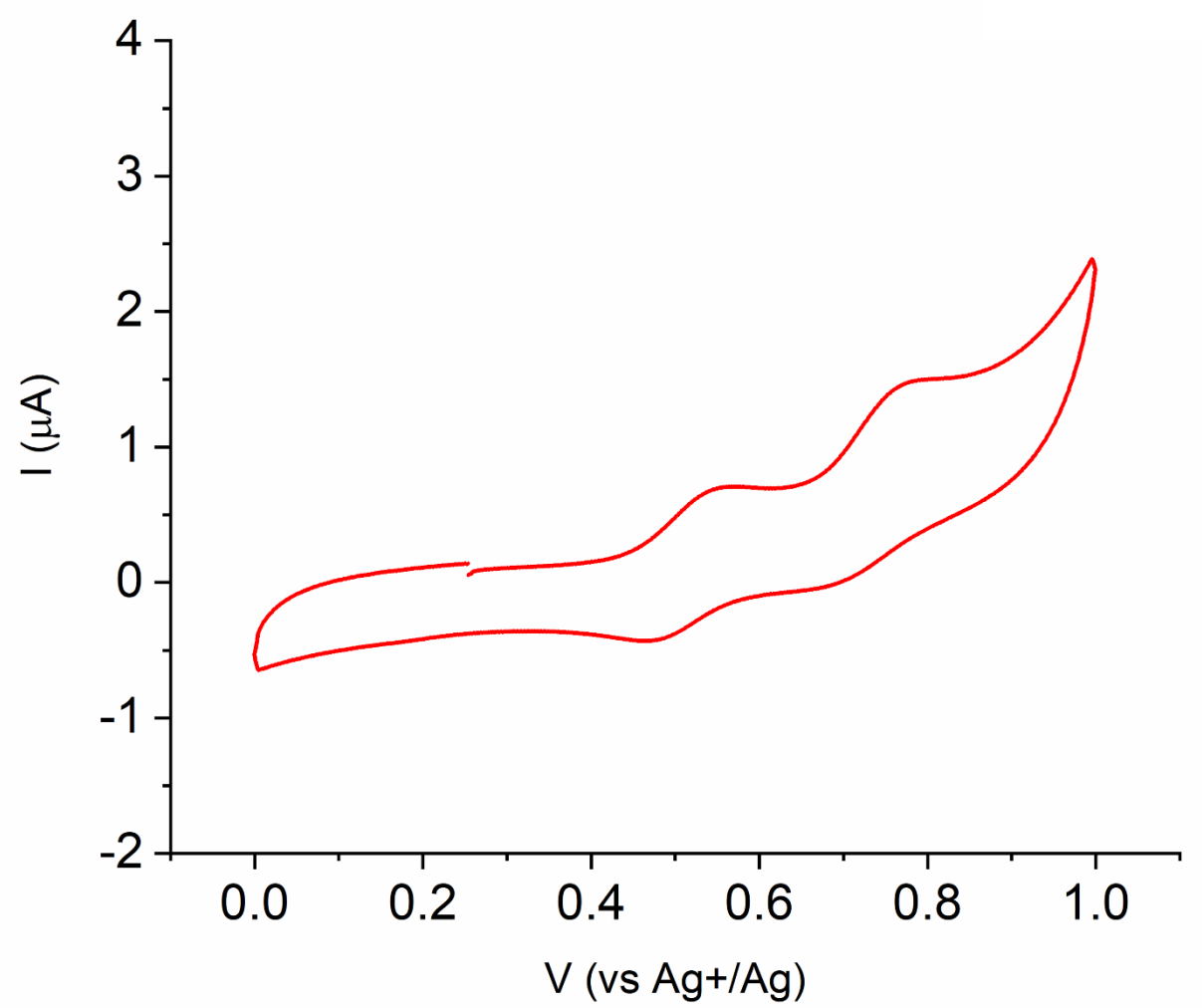

Figure S1. Cyclic voltammetry for **1-H$_4$** (0.1 M Bu_4NPF_6 in dimethylformamide; reference electrode = Ag^+/Ag, WE = Pt ; CE = Pt). Scan rate 50 $mV \cdot s^{-1}$.

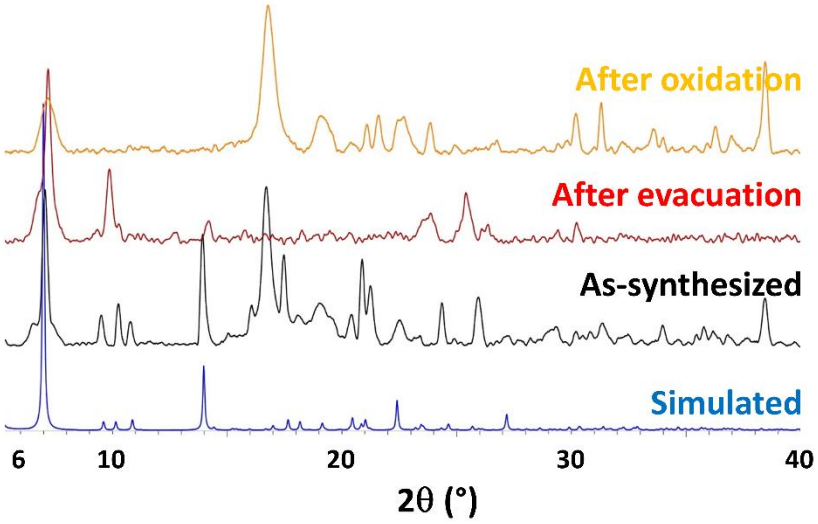

Figure S2. X-ray powder diffraction patterns for **1-Zn$_2$** simulated from SCXRD (blue), from the as-synthesized material (black), after acetone washings and vacuum drying for 12 hours (red), and after oxidation by I_2 in $CHCl_3$ (orange). The enlarged peak at 17° might arise from preferential orientation.

Table S3. Time dependency of the conductivity of an oxidized compressed pellet. The conductivity of this sample rose by a factor 40 before decreasing down to the initial value.

Time	0 h	2h15	12h	Non-oxidized sample
Conductivity (S/m)	$1.46 \cdot 10^{-5}$	$4.20 \cdot 10^{-6}$	$5.57 \cdot 10^{-7}$	$3.50 \cdot 10^{-7}$

Figure S3. Picture of the compressed pellets with the electrical contacts.

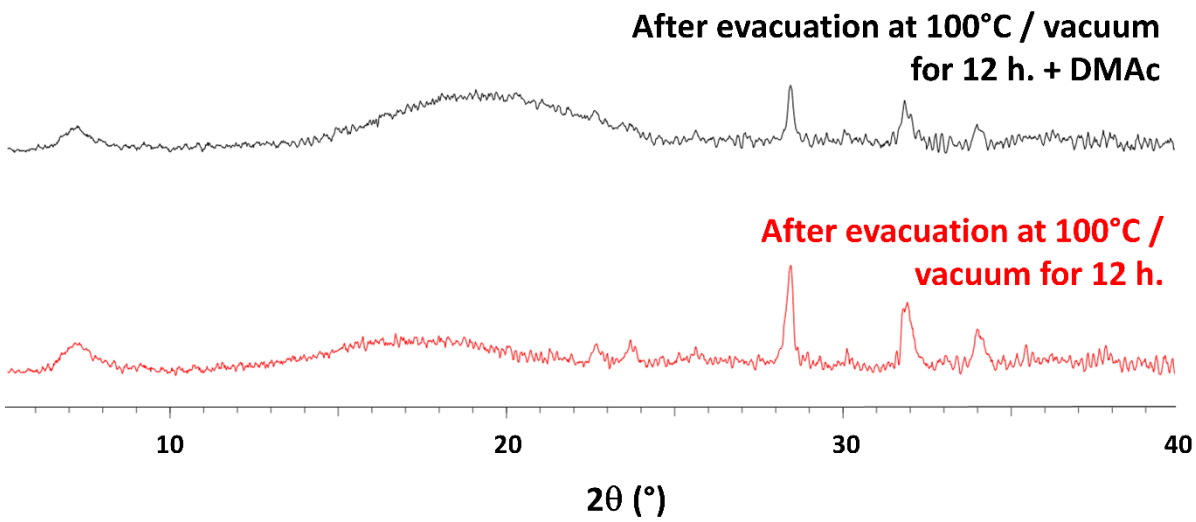

Figure S4. X-ray powder diffraction patterns for **1-Zn$_2$** after vacuum drying at 100 °C for 12h (red) and after the addition of a drop of DMAc on the amorphous powder (black). The soaking did not permit the return of the crystallinity. Peaks observed at high angle are due to NaCl and KCl impurities that recrystallized from the solvent (27.6° : NaCl (111) ; 32.0° NaCl (020) ; 34.9° KCl (110)).

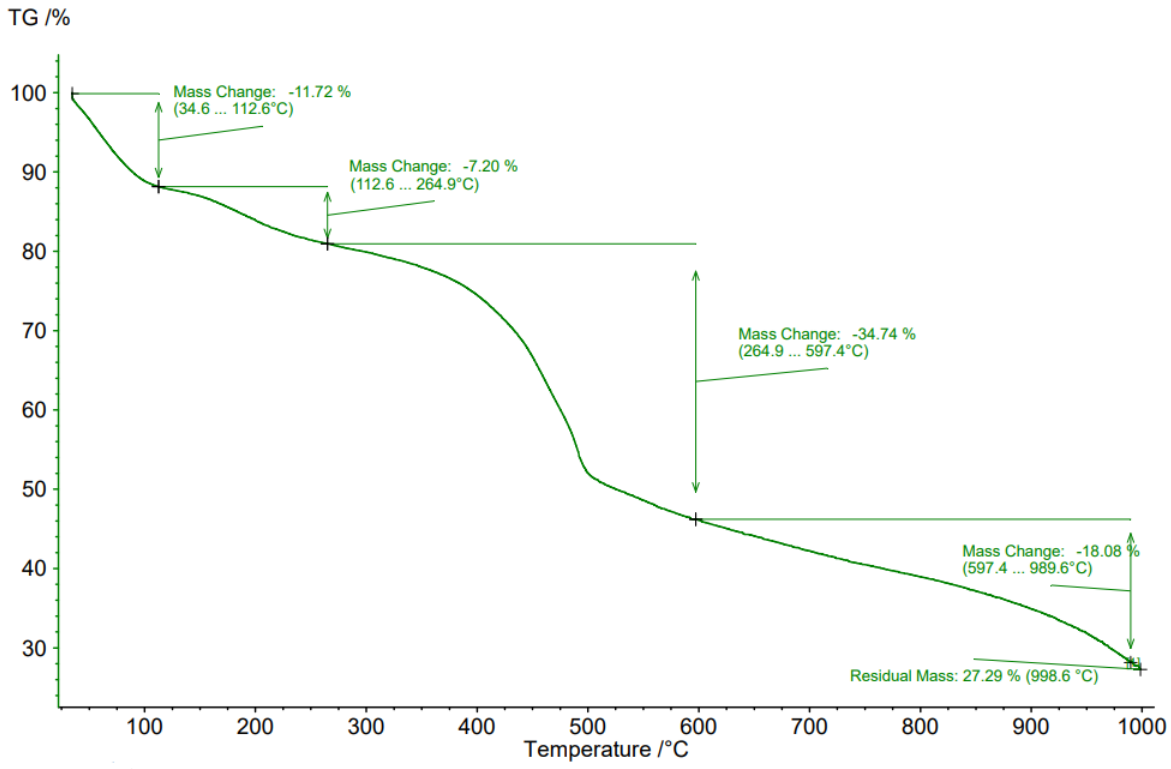

Figure S5. TGA for as-synthesized **1-Zn$_2$** (10 K/min scan-rate). The first step until 113°C corresponds to the loss of EtOH and/or water and the second until 265 °C to the loss of 1 molecule of DMAc. The material is degraded above 350°C.

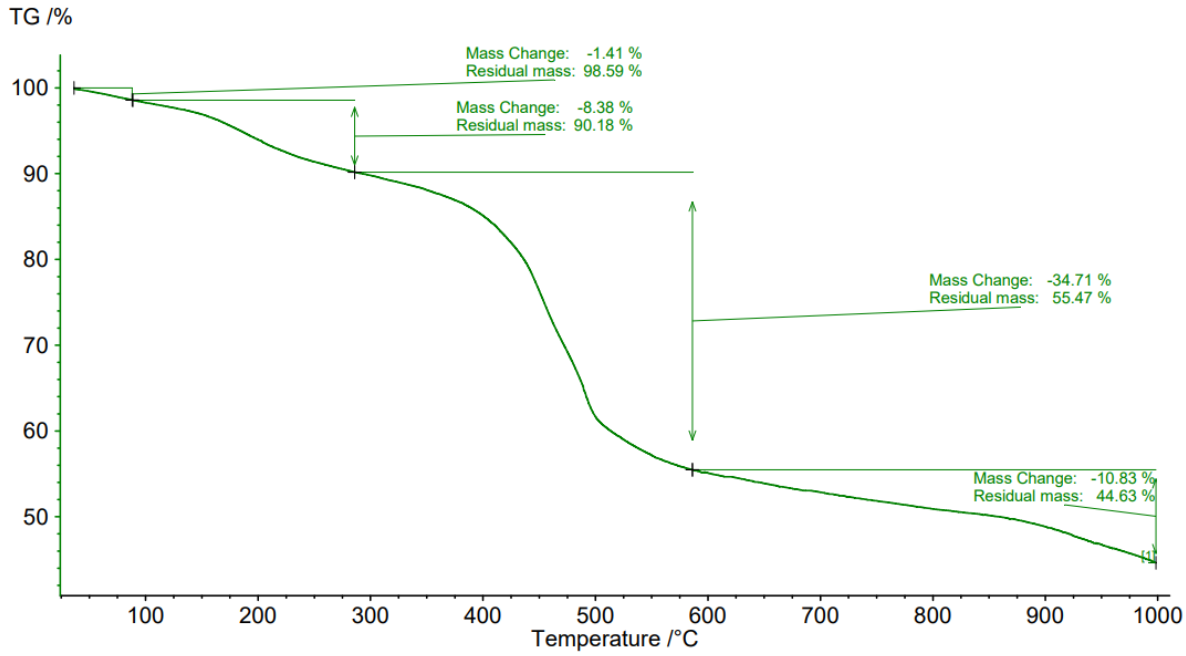

Figure S6. TGA for **1-Zn$_2$** after evacuation under vacuum at 70°C for 12h (10 K/min scan-rate). The first step until 100°C corresponds to the loss of remaining acetone molecules (*ca.* 0.3 molecule) and the second until 265 °C to the loss of one molecule of DMAc. The material is degraded above 350°C.

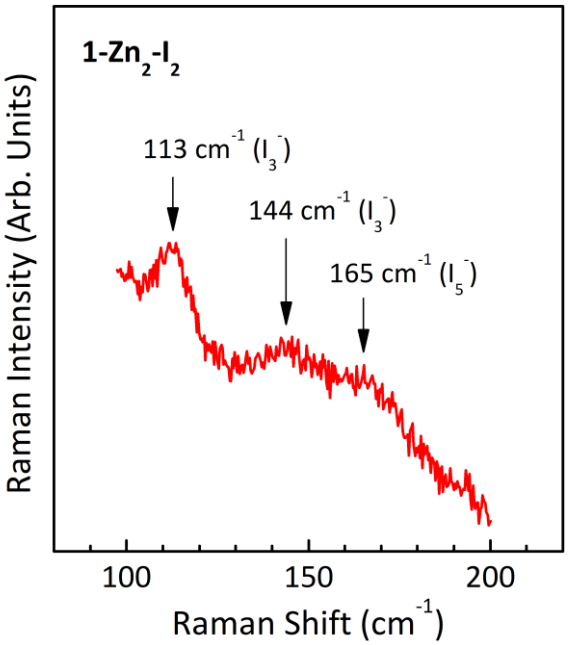

Figure S7. Raman spectrum of **1-Zn_2-I_2**, measured at room temperature with the 632.8 nm excitation line, in the frequency range of the polyiodide stretching vibrations.

Figure S7 shows the Raman spectrum of **1-Zn_2-I_2** in the frequency range of the stretching polyiodide modes. The spectrum clearly shows the symmetric stretching mode of the centrosymmetric triiodide anion centered at 112 cm^{-1}, together with the two weak features at 143 and 164 cm^{-1}, which we assign to the asymmetric stretching mode of the asymmetric triiodide ion and the symmetric stretching of the L-shaped pentaiodide ion, respectively.[11,12]

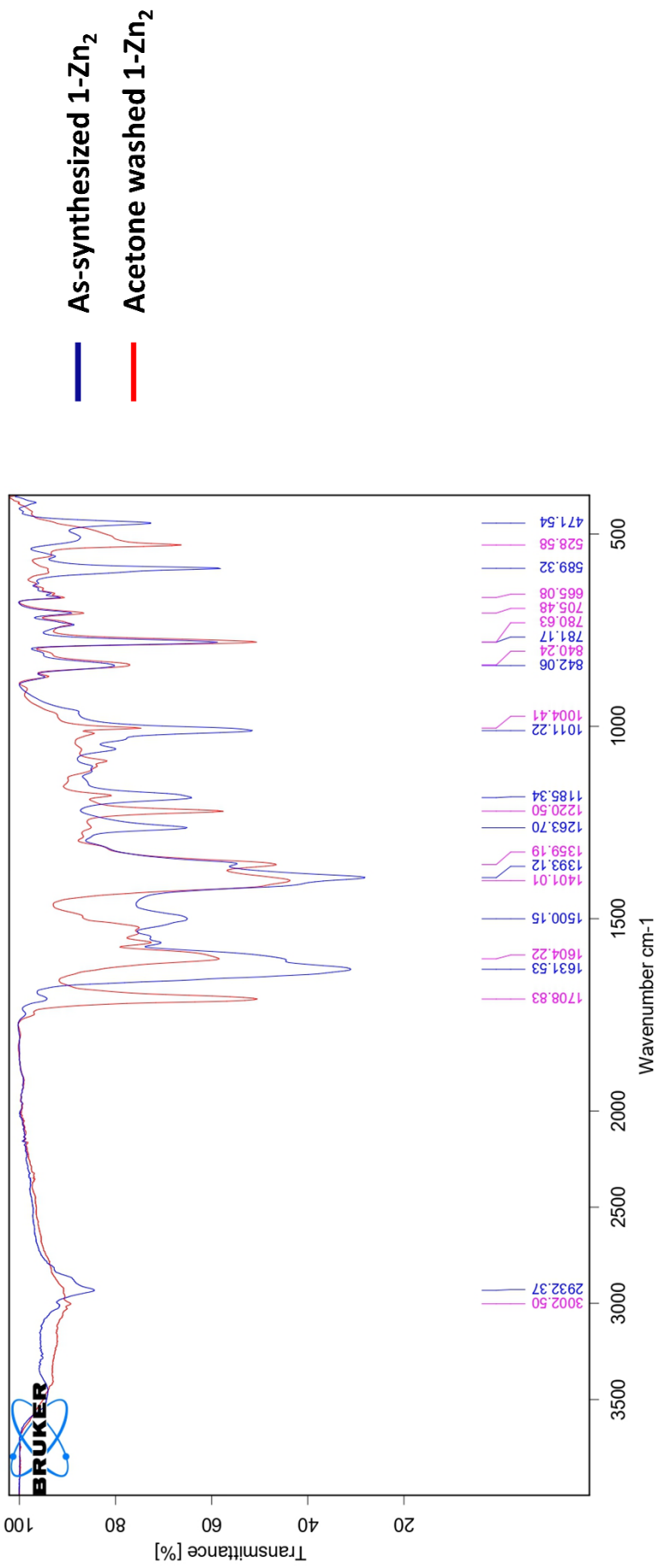

Figure S8. IR spectra before and after acetone washings for **1-Zn$_2$**. The peaks corresponding to DMAc are significantly reduced (3280 ; 2930 ; 1651 ; 1500 ; 1263 ; 1185 ; 1011 ; 590 ; 471 cm^{-1}) while peaks corresponding to acetone are observed (3002 ; 1709 ; 1359 ; 1220 ; 529 cm^{-1}).

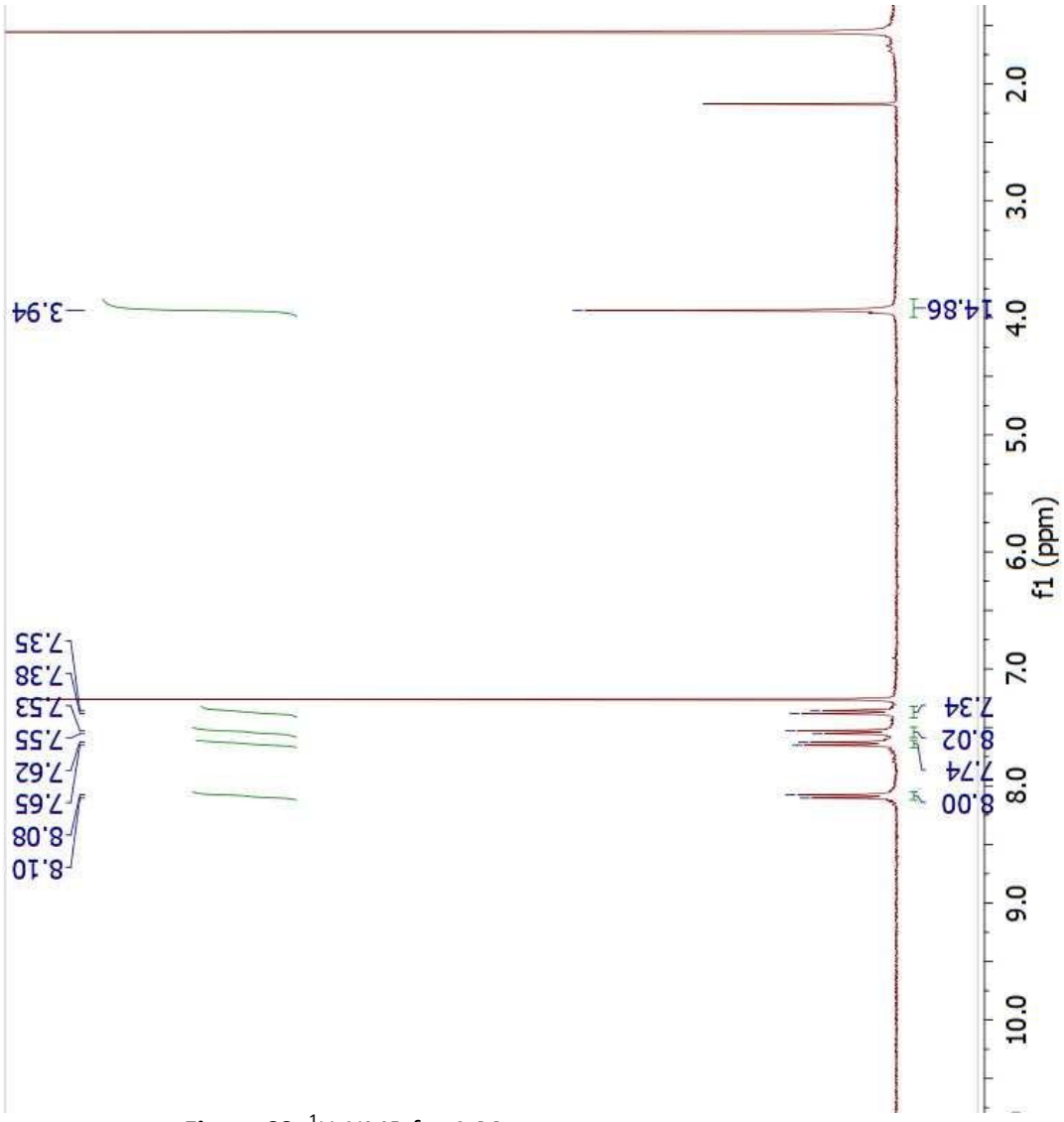

Figure S9. ^{1}H-NMR for **1-Me$_4$**.

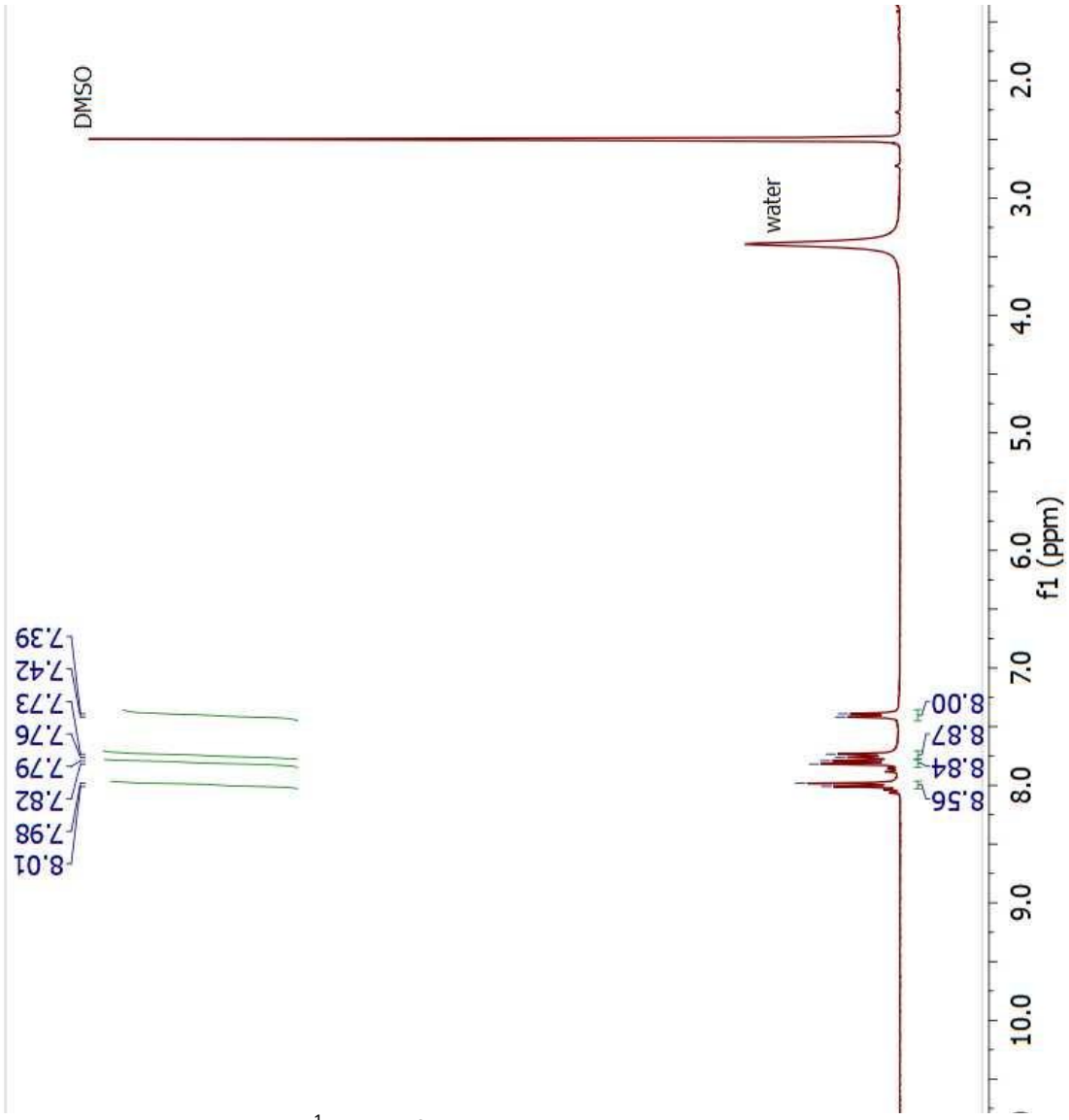

Figure S10. ^{1}H-NMR for **1-H$_4$**.

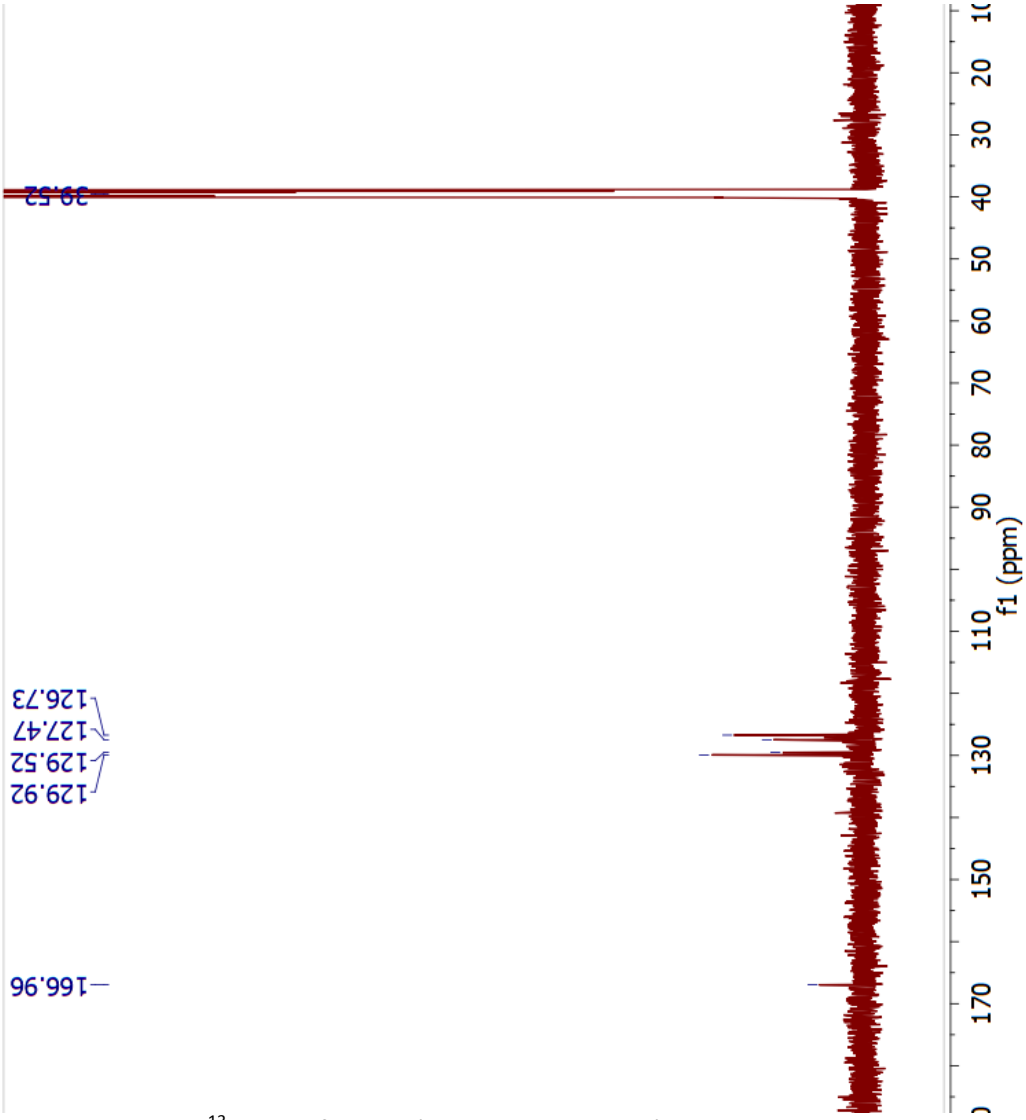

Figure S11. ^{13}C-NMR for 1-H_4 (DMSO-d_6, 125 MHz).

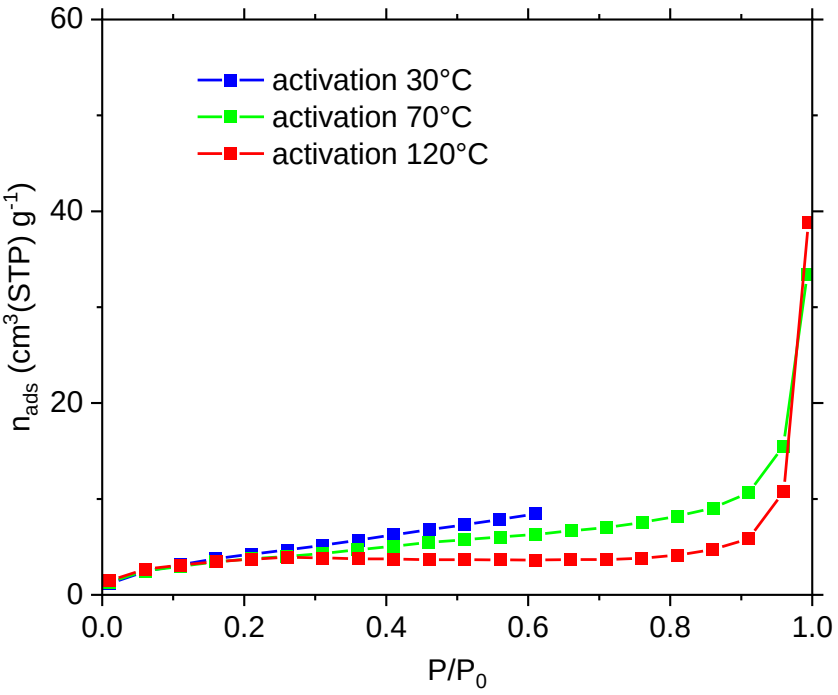

Figure S12. Nitrogen adsorption isotherms of **1-Zn$_2$** measured at 77 K after activation at various temperatures. No significant microporosity is detected.

References

1 G. M. Sheldrick, *Acta Crystallogr. Sect. A*, 2008, **64**, 112–122.
2 G. M. Sheldrick, *Acta Crystallogr. Sect. A*, 2015, **71**, 3–8.
3 C. B. Hübschle, G. M. Sheldrick and B. Dittrich, *J. Appl. Cryst.*, 2011, **44**, 1281–1284.
4 O. V. Dolomanov, L. J. Bourhis, R. J. Gildea, J. a. K. Howard and H. Puschmann, *J. Appl. Cryst.*, 2009, **42**, 339–341.
5 L.-L. Qu, Y.-L. Zhu, Y.-Z. Li, H.-B. Du and X.-Z. You, *Cryst. Growth Des.*, 2011, **11**, 2444–2452.
6 C.-H. Ma and Y.-S. Yan, *Acta Cryst. E*, 2009, **65**, m1555–m1555.
7 C. S. Hawes, N. F. Chilton, B. Moubaraki, G. P. Knowles, A. L. Chaffee, K. S. Murray, S. R. Batten and D. R. Turner, *Dalton Trans.*, 2015, **44**, 17494–17507.
8 R.-B. Fu, S.-M. Hu, H.-S. Zhang, L.-S. Wang, Y.-M. Li, X.-H. Huang and X.-T. Wu, *Jiegou Huaxue*, 2005, **24**, 1231.
9 X.-H. Zhu, X.-C. Cheng and Y.-H. Qian, *Z. Naturforsch. B*, 2017, **72**, 937–940.
10 Z. Pan, H. Zheng, T. Wang, Y. Song, Y. Li, Z. Guo and S. R. Batten, *Inorg. Chem.*, 2008, **47**, 9528–9536.
11 P. H. Svensson and L. Kloo, *Chem. Rev.*, 2003, **103**, 1649–1684.
12 I. Jerman, V. Jovanovski, A. Šurca Vuk, S. B. Hočevar, M. Gaberšček, A. Jesih and B. Orel, *Electrochim. Acta*, 2008, **53**, 2281–2288.